HEFAT2014
10th International Conference on Heat Transfer, Fluid Mechanics and Thermodynamics
14 – 16 July 2014
Orlando, Florida

EXPERIMENTAL ANALYSIS OF THE PERFORMANCE OF FRACTAL STIRRERS FOR IMPINGING JETS HEAT TRANSFER ENHANCEMENT

Cafiero G.*[,1], Discetti S[2]. and Astarita T[1].
*Author for correspondence
1 Dipartimento di Ingegneria Industriale,
Università degli Studi di Napoli Federico II,
Piazzale V. Tecchio 80, 80125
Italy
2 Aerospace Engineering Group,
Universidad Carlos III de Madrid,
Av de la Universidad 30, 28911
Spain

E-mail: gioacchino.cafiero@unina.it

ABSTRACT

A new passive method for the heat transfer enhancement of circular impinging jets is proposed and tested. The method is based on enhancing the mainstream turbulence of impinging jets using square fractal grids, i.e. a grid with a square pattern repeated at increasingly smaller scales. Fractal grids can generate much higher turbulence intensity than regular grids under the same inflow conditions and with similar blockage ratio, at the expense of a slightly larger pressure drop. An experimental investigation on the heat transfer enhancement achieved by impinging jets with fractal turbulence promoters is carried out. The heated-thin foil technique is implemented to measure the spatial distribution of the Nusselt number on the target plate. The heat transfer rates of impinging jets with a regular grid and a fractal grid insert are compared to that of a jet without any turbulator under the same condition of power input. A parametric study on the effect of the Reynolds number, the nozzle-to-plate distance and the position of the insert within the nozzle is carried out. The results show that a fractal turbulence promoter can provide a significant heat transfer enhancement for relatively small nozzle-to-plate separation (at distance equal to 2 diameters 63% increase with respect to the circular jet at the stagnation point, and 25% if averaged over an area of radius equal to 1 nozzle diameter; respectively, against 9% and 6% of the regular grid in the same conditions of power input).

1. INTRODUCTION

Cooling of turbine blades, electronic components and outer walls of combustors, paper and film drying, annealing and tempering of glass are just a few examples of applications in which the high local heat transfer of impinging jets is exploited. The transversal interest in countless industrial applications has stimulated several experimental and numerical investigations (see the reviews from Martin [1], Polat et al [2], Viskanta [3], Jambunathan [4] and O'Donovan & Murray [5]). The heat transfer is strongly dependent on the jet Reynolds number, the nozzle-to-plate distance, the angle of impingement. Other parameters, namely the jet outlet conditions and the upstream turbulence, can also have a significant effect on the spatial distribution of the heat transfer coefficients and on its value at the stagnation point.

Several solutions have been proposed over the last decades to increase and/or improve the uniformity of the distribution of the heat transfer rate of impinging jets. Among the others, acoustic excitation [6], application of swirl [7-9], introduction of perforated plates between the nozzle and the target plate [10] or installing mesh screens within the nozzle [11-12] have been investigated. In all cases the heat transfer enhancement is obtained by exciting/altering the structure and organization of large scale turbulence, which is widely recognized to be the main agent in heat and mass transfer mechanism of impinging jets [13-14]. Tampering with the large coherent turbulent structures is the key to achieve a significant heat transfer enhancement.

The effect of the upstream turbulence on the local heat transfer of single circular impinging jets is a well-known topic in the literature [5], [15-16]. Several empirical correlations

have been proposed between the Nusselt number at the stagnation point and the mainstream flow conditions (jet Reynolds number and freestream turbulence, for instance). For example, the correlation proposed by Hoogendoorn [16] for an air jet issuing from a straight long pipe is:

$$\frac{Nu_0}{Re^{1/2}} = 0.65 + 2.03\left(\frac{TuRe^{1/2}}{100}\right) - 2.46\left(\frac{TuRe^{1/2}}{100}\right)^2 \qquad (1)$$

where Nu_0 is the Nusselt number in the stagnation point, Re is the Reynolds number based on the pipe diameter d and the local streamwise velocity V, Tu is the turbulence intensity measured on the axis of the jet. The functional dependencies are essentially analogous to those found by Smith & Kuethe [17], in agreement with the intuition that pumping energy in the turbulent cascade would lead to enhanced mixing and, therefore, higher heat transfer. The turbulence intensity can be increased by inserting turbulence promoters, such as the aforementioned mesh screens. Gardon & Afkirat [18] introduced a screen into a two-dimensional slot, obtaining a significant improvement of the heat transfer in the stagnation point for relatively small nozzle-to-plate distances (for large separation the heat transfer features are dominated by the jet evolution itself, such as the entrainment and the large structures developed within the shear layer). Gori & Petracci [19] assessed the effect of the upcoming turbulence on the heat transfer of a slot jet impinging on a cylinder. The turbulence is generated by a screen placed in two locations, i.e. at the nozzle exit and at a fixed distance from the cylinder. While in the case of free jets the turbulence increases along the streamwise direction due to the interaction with the entrained fluids, and then it decreases further downstream, their results show that in presence of the grid the turbulence is built up in a production region, then it is progressively dissipated, and finally it tends to increase again due to the interaction with the stagnant air. Beyond 10 nozzle diameters, the turbulence generated by the grid is completely dissipated, and there is no significant difference between the case of the free jet and the one with turbulence enhanced by the grid.

Zhou and Lee [11] investigated the heat transfer rate of a sharp-edged orifice with a mesh screen placed $1.4d$ (d is the orifice diameter) upstream of the outflow section. Their results highlight that the achieved heat transfer enhancement is very limited (only 3.6% in the stagnation point). In a subsequent study, Zhou et al [12] have shown that a more consistent improvement can be obtained if the grid is placed right before the orifice, with an increase of about 27% of the Nusselt number in the stagnation point for a grid with blockage ratio of 25% and nozzle-to-plate distance $h/d = 0.2$.

The main conclusion of the literature survey is that it is possible to achieve a significant heat transfer improvement by increasing the turbulence intensity of the mainstream (provided that the nozzle-to-plate distance is relatively small) and that the higher is the turbulence intensity, the more intense is the heat transfer enhancement. Recently, a pioneering work by Hurst & Vassilicos [20] has shown that the low-blockage ratio fractal grids (i.e. grids with a pattern repeated at increasingly smaller scales) produce much higher turbulence intensity than regular grids with higher blockage ratios (e.g. see Figure 3 of Mazellier & Vassilicos [21]) and similar pressure drop. In particular, the turbulence generated by square space-filling (i.e. in case of infinite number of iterations the entire 2D space is filled) fractal grids is characterized by an extended production region, a peak abscissa (which is dependent on the geometrical properties of the grid) and an extremely fast decay rate, in accordance with scalings of the turbulence dissipation that are different from the ones known and widely used since the works of Taylor [35] and Kolmogorov [36] (see for example the works by Mazellier & Vassilicos [21], Seoud & Vassilicos [22], Valente & Vassilicos [23], Discetti et al [24]). The position of the peak abscissa is related mainly to the geometrical parameters of the grid, thus opening the path to proper tuning of the fractal geometry to maximize the turbulence intensity at the desired location. Fractal grids have already been used in applications in which a more intense turbulence is desirable. Geipel et al [25] used fractal cross grids to promote the turbulent strain contribution in opposed jet for combustion applications; Kinzel et al [26] investigated the effect of rotation on shear-free turbulence, and used fractal cross grids to achieve a sufficiently high level of turbulence intensity. In the scenario of impinging jets, fractal turbulence appears to be a promising system to enhance the heat transfer rate.

In this work the heat transfer enhancement of impinging jets achieved using a low-blockage ratio fractal insert is investigated. To the author's knowledge, this is the first experimental effort to quantify the features of the fractal stirrers in the improvement of the heat transfer features of impinging jets; the only contribution in this scenario is the numerical study by Laizet & Vassilicos [27] on the scalar transfer enhancement obtained by using fractal stirrers, which outlines the mechanism by which fractal grids can enhance scalar transfer and turbulent diffusion by one order of magnitude with respect to regular grids. The results of the present study are compared to those obtained by the jet without inserts (herein indicated as jet without turbulators, JWT) and by using a regular grid insert with the same blockage ratio. The comparison is conducted at the same power input (i.e. the same value of the product of the volume flow rate times the pressure drop through the nozzle). In Sec. 2 the experimental apparatus and the measurement equipment for the convective heat transfer measurement are described. In Sec. 3 the heat transfer coefficient distributions for the case of the jet without inserts and with fractal/regular inserts are compared in terms of maximum and average values of the Nusselt number and uniformity of its distribution. Finally, the results are discussed and the conclusions are drawn.

2. EXPERIMENTAL PROCEDURE

2.1 Experimental setup and measurement technique

The experimental setup is sketched in Figure 1. The air provided by a fan is conditioned in temperature with a heat exchanger and then the mass flow rate is measured with a Venturi tube. The cooling air passes through a plenum chamber (in which the total pressure is measured), a straight pipe, with length equal to $6d$ (where d is the exit diameter, equal to

$20mm$) and, if present, through the insert and a terminating cap. The air impinges normally on a thin constantan foil ($200mm$ long, $450mm$ wide, $50\mu m$ thick), which flatness is ensured by a stiffening frame. The separation (indicated with the symbol h) of the nozzle exit section from the target plate is adjusted by using a precision translation stage to move the jet plenum chamber along its own axis perpendicular to the heated surface. The target plate is heated by an electric current and cooled by the jet impinging on it. The grid insert is placed within a small cavity shaped into a cap that is attached to the straight pipe (see the insert of Figure 1 for the graphical representation). The depth of the cavity is equal to the grid thickness, i.e. $0.5mm$. Three caps with a total height of $1.5, 10.5$ and $20.5mm$ have been used, thus corresponding to $z = 0, 10$ and $20mm$ respectively. The smallest cap is knife-edged close to the grid location (with angle of 45°) to reduce its influence and reproduce the condition of grid placed at the nozzle exit. It is helpful to explicitly notice that the grid is always placed at the end of the straight pipe for all the values of z. More specifically, this results in the condition that the grid is practically in correspondence of the nozzle exit when the smallest cap is used (i.e. $z/d = 0$), whilst it is upstream of the nozzle exit in the other cases (i.e. $z/d = 0.5, 1$), thus with a total pipe length of $6.5d$ and $7d$ respectively. When testing the JWT the terminating cup is not used, thus the obtained results are relative to the case of outflow from a straight pipe with $6d$ length.

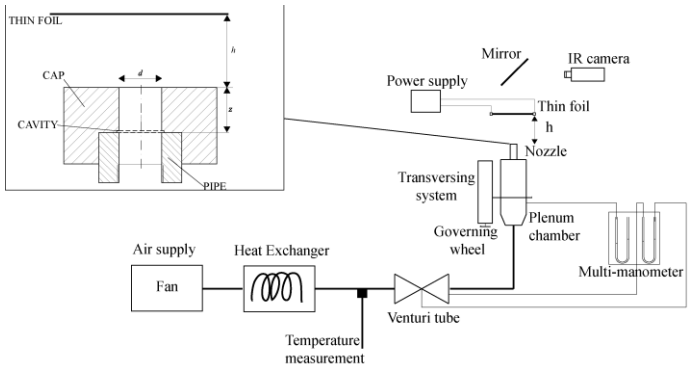

Figure 1 Experimental setup and detail (insert) of the item used to set the grid to nozzle exit section distance

The temperature of the foil is measured by an InfraRed (IR) camera FLIR SC6000 (focal plane array with 640x512 pixels working in the $8 - 12\mu m$ band). The camera is placed at the opposite side to that of impingement; this is acceptable being the Biot number ($Bi = h_c s/k_f$, where s is the foil thickness, k_f is the thermal conductivity of the foil and h_c is the convective heat transfer coefficient) lower than 0.01 for the entire set of experiments, so that the temperature can be considered uniform across the foil thickness with good approximation. The back side of the foil (i.e. the one opposite to the impingement area) is covered with high emissivity paint ($\varepsilon = 0.95$) in order to increase the signal/noise ratio with respect to the radiation coming from the surrounding ambient. The temperature map is discretized with a resolution of $3.2pix/mm$, thus corresponding to $64pix/d$.

The convective heat transfer coefficient is evaluated via the *heated thin foil* steady state heat transfer sensor [30]. The heated thin foil sensor provides the time-averaged convective heat transfer coefficient between a thermally thin foil (i.e. with reasonably small Bi) with uniform external heating (for example provided by Joule effect) and the air impinging on it. The distribution of the convective heat transfer coefficient is obtained by applying the steady-state energy balance to the foil, as sketched in Figure 2. The final result is the formula:

$$h_c = \frac{\dot{q}_j - \dot{q}_r - \dot{q}_{nc} - \dot{q}_{tc}}{T_w - T_{aw}} \quad (2)$$

The convective heat flux is expressed in terms of the Newton's law, thus leading to the difference of the wall temperature T_w and the adiabatic wall temperature T_{aw} in the denominator on the right hand side of Eq. 2. The other terms in Eq. 2 represent respectively:

- $\dot{q}_j$: heat flux input provided by Joule effect;
- $\dot{q}_r$: radiative heat flux towards the flowing fluid. This contribution is neglected on accord to its very small value while the one towards the ambient is estimated via the so-called radiosity law:

$$\dot{q}_r = \gamma\varepsilon(T_w^4 - T_a^4) \quad (3)$$

where γ is the Stefan-Boltzmann's constant and T_a is the ambient temperature; this contribution for the entire data set does not exceed 7% of the $\dot{q}_j$ value;

- $\dot{q}_{nc}$: natural convection heat flux. It can be estimated using the well-consolidated empirical correlations reported in the literature (see Incropera et al [31] and McAdams [32] among the others). In the present experiments it never exceeds 6% of the convective heat transfer; this yields to a corresponding natural convection Nusselt number equal to about $Nu_{nc} \approx 10$;
- $\dot{q}_{tc}$: thermal losses due to tangential conduction. For the simplified case of isotropic material, this term can be estimated by multiplying the Laplacian of the wall temperature for the thermal conductivity of the material as in Astarita et al [33]:

$$\dot{q}_{tc} = k_f s \nabla^2 \mathrm{T_w} \quad (4)$$

As suggested by Carlomagno et al [34], it is highly recommended to filter the temperature maps to reduce the effects of the measurement noise and of the residual error after the non-uniformity correction of the focal plane array. In this application a least square 2nd order polynomial fitting on 5x5 pixels kernels is applied. However, the contribution of the tangential conduction is less than 1% of the $\dot{q}_j$ value for the entire data set.

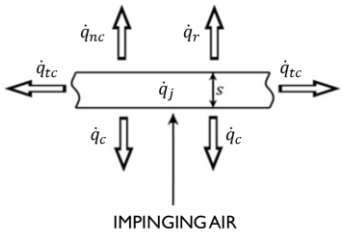

Figure 2 Sketch of energy balance of the foil

In each experiment the adiabatic wall temperature T_{aw} is measured by taking the temperature maps of the target plate with the impinging jet on it and the electric current input off. This map is commonly referred to as "*cold image"*. The corresponding "*hot image*" is recorded by imposing an electric power input large enough to provide a temperature difference of at least $15K$ between T_w and T_{aw} in all the points of the impinged plate. The difference between the hot and the cold image, corrected with the possible ambient temperature change is, as a matter of fact, the denominator of Eq. 2. Each temperature map is obtained by averaging 1000 recorded images at a frame rate of $30Hz$. The integral timescale is well below the time separation between the frames (in the worst case the jet bulk velocity is $12m/s$, thus considering that the nozzle diameter is $20mm$ it leads to a timescale equal to $1.6ms$, against $33.3ms$ between two consecutive frames), thus the samples can be considered statistically independent. Only time-averaged results are reported since the thermal inertia of the foil does not allow to accurately follow the turbulent fluctuations in the instantaneous realizations. Indeed, considering the foil thickness as the reference length across which the heat is transferred by conduction, the characteristic time obtained by setting the Fourier number equal to 1 is $0.45ms$, while the estimated Taylor and Kolmogorov timescales are respectively $100\mu s$ and $8\mu s$.

The convective heat transfer coefficient is presented in dimensionless form in terms of the local Nusselt number:

$$Nu = \frac{h_c d}{k} \tag{5}$$

where k is the thermal conductivity of the fluid. The results are reported in terms of radial profile of the azimuthal and integral average of the Nusselt number, as defined in the following:

$$Nu_r(r) = \frac{1}{2\pi}\int_0^{2\pi} Nu(r,\alpha)d\alpha \tag{6}$$

$$\overline{Nu}(r) = \frac{1}{\pi r^2}\int_0^{2\pi}\int_0^{r} Nu(\rho,\alpha)d\rho d\alpha \tag{7}$$

The two parameters give a direct grasp on the local mean value and the integral of the convective heat transfer over a considered area, respectively.

An uncertainty analysis on the values measured by the Eq. (2) is conducted as suggested by Moffat [35]. The uncertainties in the foil properties (thickness), the emissivity of the black paint, the measured ambient and foil temperature, the input current and voltage are the main contributions. The analysis leads to a $\pm 4.2\%$ range of uncertainty for the local Nusselt number. In Table 1 the typical value and the uncertainty associated to each parameter that has been taken into account for the Nusselt number computation together with the effective percentage of error that it introduces in the measure are reported. It can be concluded that the main effect on the Nusselt number estimate is related to the adiabatic wall temperature measure. The total error is then estimated as the root sum square of the single errors. Besides the errors listed in Table 1, there is also the one related to the pressure measurement (estimated to be about 2% of reading), which has not a direct effect on the Nusselt number definition.

The experiments are performed by varying both the nozzle-to-plate distance ($h/d = \{1,2,3,4\}$) and the position of the grid with respect to the nozzle exit ($z/d = \{0,0.5,1\}$). Only relatively short nozzle-to-plate distances are considered; indeed, in this scenario the effect of the enhanced turbulence within the potential core is dominating. For larger separations the large-scale disturbances generated within the shear layer are expected to have an overwhelming impact on the heat transfer properties, while the grid-generated turbulence in the potential core is smeared out by diffusion.

	Typical Value	**Uncertainty**	$\left(\frac{\partial R_i}{\partial X_i}\frac{\delta X_i}{Nu}\right)\times 100$
T_w	$304\ K$	$200\ mK$	2.3
T_{aw}	$293\ K$	$200\ mK$	2.7
T_a	$293\ K$	$0.1K$	1.4
I	$63\ A$	$1\%\ of\ reading$	1.0
V	$1.40\ V$	$1\%\ of\ reading$	1.0
ε	0.95	0.01	0.06
d	$0.02\ m$	1%	1.0
s	$50\ \mu m$	1%	10^{-5}
Err			4.2

Table 1 Error analysis according to Moffat [35]

2.2 Fractal insert and tests configuration

A sketch of the fractal insert is reported in Figure 3. The insert is made of a $0.5mm$ thick aluminum foil; the fractal structure is shaped by laser cutting. The square pattern is repeated at three different scales (commonly referred as iterations). The length L_0 and the thickness t_0 of the first iteration are equal to $10mm$ and $1mm$, respectively. At each iteration j the length L_j and the thickness t_j are halved, i.e. $L_j = L_0 R_L^j$ and $t_j = t_0 R_t^j$, with $R_L = R_t = 1/2$. For this grid the ratio between the largest and the smallest bar thickness (i.e. the thickness ratio t_r, identified as a significant scaling parameter by Hurst & Vassilicos [20]) is equal to 4. The blockage ratio of the grid is equal to 0.32. Using the scaling relations by Hurst & Vassilicos [20], an "equivalent" regular grid is designed (i.e. with the same blockage ratio σ and effective meshlength M_{eff}):

$$M_{eff} = \frac{\pi d^2}{P}\sqrt{1-\sigma} \tag{8}$$

$$\sigma = \frac{b}{M}\left(2 - \frac{b}{M}\right) \quad (9)$$

with P and b being the grid perimeter's length and the bar thickness, respectively The meshlength of the regular grid is equal to 2.4mm, while the bar thickness is $0.4mm$.

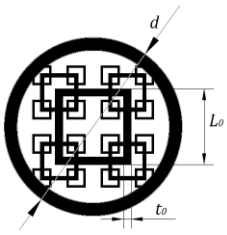

Figure 3 Sketch of the fractal insert

The experiments are carried out at nominal Reynolds numbers equal to 16,000 and 28,700 (using the following expression based on the flow rate $Re = \frac{4\rho Q}{\pi \mu d}$). Considering that the presence of the insert and its position with respect to the nozzle exit have a significant influence on the pressure drop, the tests are conducted with the same power input, i.e. the product of the pressure drop and the volumetric flow rate is kept constant ($1.1mW$ and $5.5mW$ for the two cases, respectively). For this reason, the test Reynolds number (referred to as "nominal" Reynolds number in the following) is related to the reference case of fractal grid located at the exit section, i.e. $z = 0$ (i.e. the case with the largest pressure drop and, consequently, the lowest flow rate within the data set of each test Reynolds number). From this point on, comparison will always be performed at the same power input, i.e. same nominal Reynolds number, but the effective Reynolds number based on the flow rate and the jet diameter will be different. The effective Reynolds numbers of all the test cases are reported in the Tables 2-3.

	JWT			Regular grid			Fractal grid		
	$Q[g/s]$	$\Delta p[N/m^2]$	Re	$Q[g/s]$	$\Delta p[N/m^2]$	Re	$Q[g/s]$	$\Delta p[N/m^2]$	Re
$z = 0$	6.3	178	23200	4.8	229	17900	4.3	237	16000
$z = 0.5d$				4.9	220	18000	4.9	229	18000
$z = 1d$				4.9	220	18000	5.0	220	18600

Table 2 Mass flow rate, pressure drop and Reynolds number for the test case with power input of $1.1mW$

	JWT			Regular grid			Fractal grid		
	$Q[g/s]$	$\Delta p[N/m^2]$	Re	$Q[g/s]$	$\Delta p[N/m^2]$	Re	$Q[g/s]$	$\Delta p[N/m^2]$	Re
$z = 0$	10.4	535	38500	4.8	229	17900	4.3	237	16000
$z = 0.5d$				4.9	220	18000	4.9	229	18000
$z = 1d$				4.9	220	18000	5.0	220	18600

Table 3 Mass flow rate, pressure drop and Reynolds number for the test case with power input of $5.5mW$

3. RESULTS

3.1 Nusselt number distributions

In Figure 4 the convective heat transfer coefficient distributions, for the jet without turbulators (JWT), the Regular Grid (RG) and the Fractal Grid (FG) cases, are reported in non-dimensional form for power input of $5.5mW$, i.e. nominal Reynolds number equal to 28,700 (evaluated for the case of the fractal insert at the nozzle exit section; please refer to Table 3 for the effective Reynolds number of the other cases).

The contour plots for the JWT are reported in Figures 4a-c for three nozzle-to-plate distances. The maps reveal a double-peak shape of the radial distribution of the Nusselt number, i.e. the convective heat transfer rate reaches a local minimum at the stagnation point; then it increases with the radial distance up to $\frac{r}{d} \approx 1$; again, the heat transfer rate decreases with the radial separation and reaches a second local minimum at $\frac{r}{d} \approx 1.5$; beyond that point, it increases up to $\frac{r}{d} \approx 2$, where the Nusselt number achieves a local maximum; then, for larger radial separation, the heat transfer rate decreases monotonically. This pattern is a well-known feature for small nozzle-to-plate distances, and it is commonly addressed to the formation of ring vortices within the jet shear layer due to the entrainment in correspondence of the nozzle exit section. By looking at the Nusselt number values at the stagnation point reported in Figure 5 for an easier identification, an improvement in the heat transfer rate can be detected as the nozzle-to-plate distance increases. This effect should be visible up to distances of $h/d = 7.5$ (see [3-5]), where the effect of turbulence enhancement is not capable anymore to compensate for the decay of the jet velocity and, consequently, the Nusselt number in the stagnation point falls down rapidly.

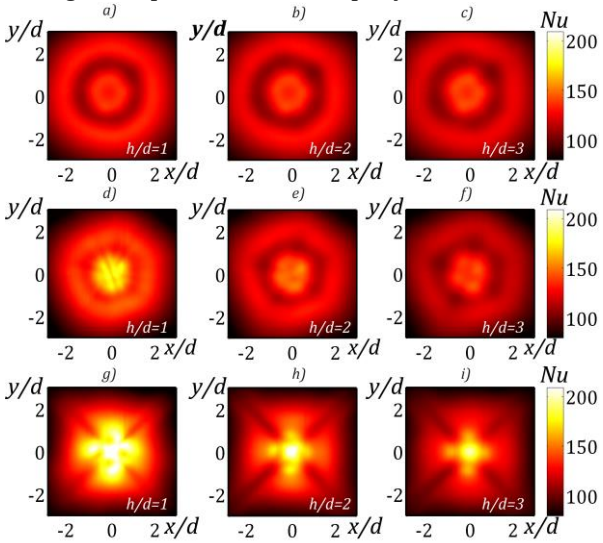

Figure 4 Nusselt number maps for the jet without turbulators (JWT, *a* to *c*), the regular grid (RG, *d* to *f*) and the fractal grid (FG, *g* to i). The test conditions are: nominal Reynolds number 28,700, grid located at the nozzle exit ($z/d = 0$). For the effective Reynolds number of JWT and RG please refer to Table 3

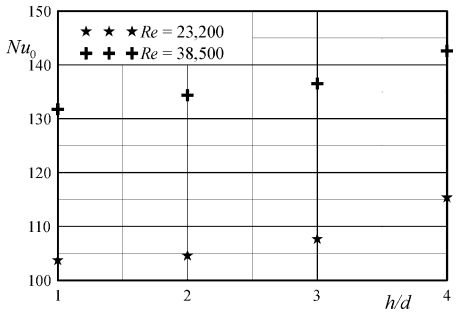

Figure 5 Nusselt number values at $r/d = 0$ for the JWT case

The Nusselt number maps for the RG case are reported in the second row of Figure 4 (*d* to *f*). The axial symmetry in the heat transfer rate is perturbed by the regular insert, which acts similarly to a multi-channel. The mesh "print" on the impinging surface is detectable on the maps (even though it is not completely resolved due to the limited spatial resolution). Moreover, the Nusselt number does not decrease as the radial distance increases; in fact, similarly to what observed for the JWT case, for small h/d values at radial separation from the axis equal to about $r/d \approx 2$ the Nusselt number increases again attaining a second local maximum. On the other side, the behaviour result to be different from the JWT case as h/d increases; the heat transfer rate result to be monotonically decreasing, as it will be shown in the next section, up to $h/d = 3$. For larger separations, an increment in the Nusselt number can be still detected in correspondence of the stagnation region.

The third row in Figure 4 (*g* to *i*) reports the Nusselt number maps for the FG case. The phenomenology is completely different from the previous cases. The contour plot reports a maximum value of the heat transfer rate located at the stagnation point that is much larger than the other cases; interestingly enough, the improvement in the heat transfer rate is mainly related to the central zone of the jet, whilst for larger radial separations from the jet axis, the Nusselt number values are quite similar to those of the JWT and RG cases. Furthermore, as already outlined for the RG case, local maxima are also present at a distance from the nozzle axis of about $1d$. However, the remarkable gap in the absolute heat transfer rate (even though the test Reynolds number of the RG is larger than that of the FG) spotlights relevant differences.

The striking difference might be addressed to the different turbulence-generation mechanism of fractal and regular grids. As already outlined in the numerical simulations by Laizet & Vassilicos [29], the fractal generated turbulence enhances the scalar transfer according to a space-scale unfolding (SSU) mechanism, i.e. the wakes with different size generated by the fractal stirrer meet at different downstream locations. In this scenario an individual fluid particle might jump into a larger wake and experience an eddy turnover time larger than that of the original wake (see [29] for a more exhausting treatment). This mechanism is absent in regular grids, where all the wakes have similar size and meet immediately beyond the grid; this yields to a more intense turbulence production in a short space confined in proximity of the grid, and a subsequent rapid decay. The strong confinement of the high turbulence intensity region of regular grids obstructs its usage for application purposes or turbulence modelling, while the geometry of fractal grids can be tuned to relocate the turbulence intensity peak, thus enabling its exploitation. The SSU would explain the high persistence of enhanced turbulent diffusion downstream of the grid, and, consequently, the higher heat transfer rate.

The qualitative sketch reported in Figure 6, in which the fractal grid is superimposed to the Nu map, might be helpful to highlight some interesting features of the Nusselt number distribution for the case of the jet with fractal insert. The stagnation region Nusselt number peak is related to the acceleration of the fluid issued through the largest square of the grid (i.e. the first fractal iteration). The jet velocity increases (as it experiences a sudden contraction) as well as the "effective" local Reynolds number, causing an improvement in the convective heat transfer efficiency. In the cited figure, this zone is identified by the tag "local acceleration". This phenomenon is also present in correspondence of the "holes" between the squares of the second and third fractal iteration and the external skeleton of the insert, as indicated in the figure where other local maxima are present. In the wake of the smallest iterations, the heat transfer rate achieves lower values due to the locally higher blockage ratio. As the nozzle-to-plate distance increases (in Figure 4 at $h/d = 3$) the outer peaks merge with the local maximum in the stagnation region, determining a cross-shaped Nu distribution. This interaction might be addressed due to the turbulent diffusion, which at a sufficient streamwise distance is expected to smear out the wakes of the fractal iterations and the central jet.

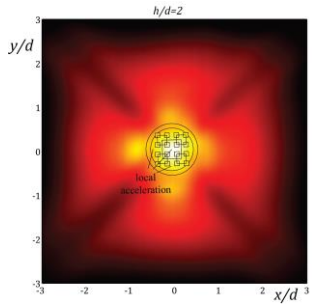

Figure 6 Qualitative representation of the effect of the fractal grid geometry on the Nusselt number distribution

In order to highlight the effect of the position of the grid insert with respect to the nozzle exit section, the Nusselt number distributions for inflow conditions with a nominal Reynolds number $Re = 28{,}700$ keeping constant the power input are reported in Figure 7 in the cases of grid located at $z = 0.5d$ and $z = 1d$ (see Table 3 for the corresponding values of the effective Reynolds number). The phenomenology sensibly varies as the insert is moved upstream in the nozzle. Indeed, the presence of the straight tube mitigates the efficiency of the grid in turbulence production. In particular, two effects are clearly visible looking at the maps of Figure 4, 7: firstly, as it will better illustrated in Sec. 3.2, for small nozzle to plate separations, the Nusselt number in the stagnation region is quite similar for the three cases (see Figure 4*g* and Figures 7*a* and *7d*). This feature has to be addressed to the progressive enhancement of the heat transfer rate that may be achieved as

the nozzle-to-plate distance approaches the distance where the turbulence generated to the fractal stirrer would be maximum in free shear conditions (see Sec. 3.2.1 for further details). This element is even more interesting considering that the pressure drop due to the presence of the fractal insert progressively decreases as the grid is moved within the nozzle (see Tables 2, 3). Secondly, although the nozzle exit section to plate distance does not vary with respect to the case of grid set at the nozzle exit section, differently from the case of Figure 4 (g to i), the mixing of the stagnation region with the outer maxima occurs at lower values of h/d (in both cases, $h/d < 2$).

In order to better illustrate the feature of the non-axial-symmetric Nusselt number distribution of jets with fractal grids, the Nusselt number profiles at α =0°, 45° (where α is the angle between one of the two axis of symmetry directed as the square sides of the FG, named x axis, and the generic direction in a polar system) obtained by averaging the 1000 realizations over time (solid lines) are reported; the azimuthal average (Nu_r, dashed line) of the Nusselt number distribution is also plotted for clarity. It is evident that the second maximum in the

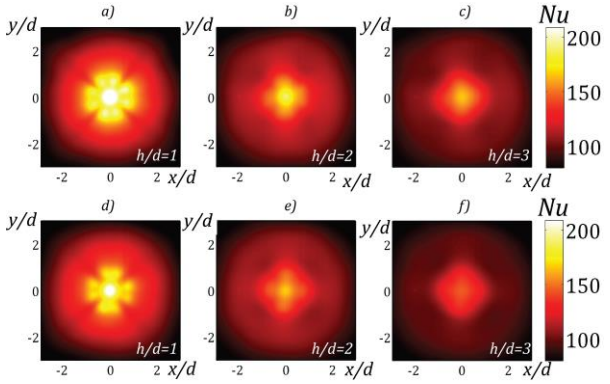

Figure 7 Nusselt number maps for the fractal grid (FG). The test conditions are: nominal Reynolds number 28,700, grid located at $0{,}5d$ (a, b, c) and $1d(d, e, f)$ from the nozzle exit section. For the effective Reynolds number of the test cases please refer to Table 3

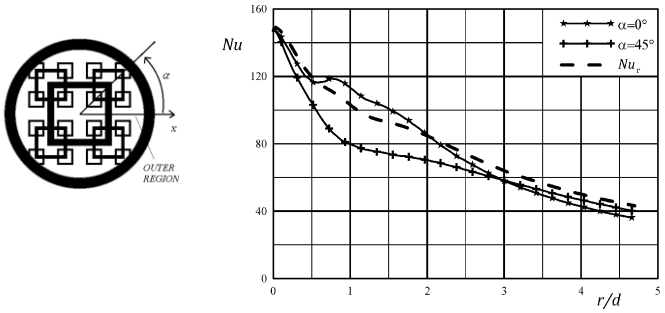

Figure 8 Polar reference system (left) and Nusselt number distribution (right) for the FG case; $Re = 28{,}700$, $z/d = 0$, $h/d = 2$. The dashed line represents the azimuthal average

Nusselt number distribution is only present along the $\alpha = 0°$ direction. This region corresponds to the one contained between the outer iterations and the external circle (labeled as outer region in Figure 8, left), where the issuing jet experiences a sudden acceleration. Along the $\alpha = 45°$ direction the profile results to be monotonically decreasing and this reflects also in the azimuthal average, where the effect of the acceleration through the external regions is smeared out by the average operation.

3.2 Nusselt number distributions

In this section, the effect of the main parameters influencing the convective heat transfer rate will be analyzed. The following parameters will be considered as reference conditions:

- $h/d = 2$;
- nominal $Re = 28{,}700$;
- $z/d = 0$.

In each subsection the effect of each single item will be discussed in order to isolate the respective influence on the Nusselt number distribution, while the other two parameters will be kept constant at the reference condition.

3.2.1 Effect of the nozzle to plate distance (h/d)

In Figure 9 the profiles of the spatially averaged Nusselt number (Eq. 7) are plotted as a function of the radial distance; plots are reported for $h/d = \{1, 2, 3, 4\}$. The behavior of the fractal insert is quite different from both the JWT and the regular grid. Indeed, for the FG case the convective heat transfer rate at the stagnation point monotonically decreases with the nozzle to plate distance. This is not true in the case of the JWT: as already outlined in Sec. 3.1 (see Figure 5). For the RG, especially for larger nozzle-exit to plate distances, there is the clear presence of a maximum in the radial distribution at $r/d \approx 0.4$ for $z/d = 0$. Actually, as outlined in Figure 7, a double-peak shape can be observed also in some Nusselt number radial profiles for the case of the fractal grids; however, this effect occurs at small radial separation from the jet axis ($r/D \approx 0.75$), and it is reasonably to be addressed to the defect of velocity in the wake of the largest fractal iteration. Furthermore, when integrated over an area, as in Figure 9, this effect is on average deleted.

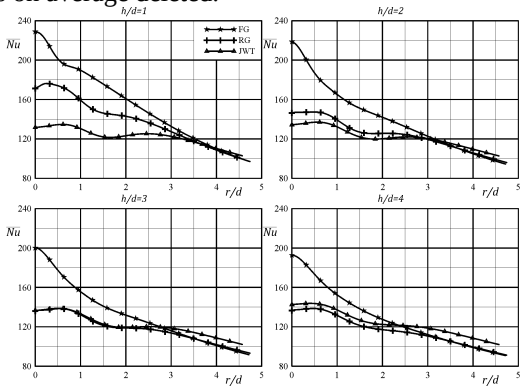

Figure 9 Nusselt number distribution for nominal Reynolds number$Re = 28{,}700$, $\frac{z}{d} = 0$, $\frac{h}{d} = \{1, 2, 3, 4\}$ and constant value of the power input equal to 5.5 mW(see Table 3 for the effective Reynolds number values)

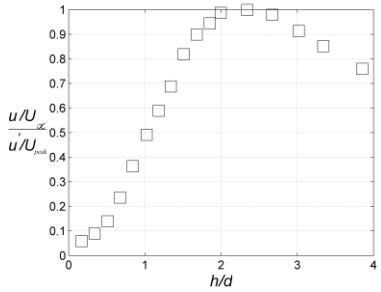

Figure 10 Fractal generated turbulence decay law (extracted from Figure 39 of Hurst & Vassilicos [20])

Interestingly enough, the gap between the FG and the other elements decreases as h/d increases; in other words, the fractal insert is more efficient in the case of small distances. One possible interpretation of this aspect might be addressed to the peculiar features of the mechanism of turbulence generation and decay of fractal grids. An example of streamwise turbulence intensity profile is extracted from Figure 39 of Hurst & Vassilicos [20] and plotted as a function of the streamwise coordinate (in this case the nozzle-to-plate distance). Fractal grids generate an elongated production region, where the turbulence builds up until it reaches the maximum value at a coordinate that is related to the characteristics of the first iteration of the grid. The position of the turbulence intensity peak can be estimated as $x_{peak} \approx 0.45x^*$, where $x^* = L_0^2/t_0$ is referred to as wake-interaction lengthscale [21]. For the tested fractal geometry $x^* = 100mm$, thus the peak of the turbulence intensity could be expected at about $(h+z)/d \approx 2 \div 2.5$. Of course the profile of Figure 10 is relative to the very different condition of free shear flow, but it still can provide a significant qualitative reference point in the interpretation of the results: in fact, it should be reasonable to presume that the turbulence intensity peak occurs in the case of impinging jet at lower nozzle to plate separations. The extremely fast decay of the intensity of fractal turbulence [25] can explain why the gap between the heat transfer of FG and that of both the RG and JWT drops down rapidly with increasing h/d.

3.2.1 Effect of the position of the grid within the nozzle (z/d)

The spatially averaged Nusselt number profiles are illustrated in Figure 11 for the three tested locations of the insert within the nozzle. For the same value of the power input, the highest value of the heat transfer rate can be detected in correspondence of the stagnation region when the grid is located at $z/d = 0.5$. As remarked before, this effect might be addressed to the fact that the maximum turbulence intensity is achieved for $(h+z)/d \approx 1.5$. When this distance increases, the turbulence produced by the grid is lower and consequently the heat transfer efficiency decreases as well.

However, it has to be pointed out that this effect is characteristic of the stagnation region; in fact, for $r/d > 1$, although very similar values are measured, the configuration with the grid set at the nozzle exit section reveals to be the most efficient. Finally, the Nusselt number profiles for $z/d = 0.5, 1$ result practically coincident for $r/d > 3.5$, i.e. in the wall jet region.

Considering that in the case of $z/d = 0.5$ the achievable heat transfer rate is larger that the other cases at least for small nozzle to plate separations, it can be speculated that the enhancement due to fractal stirrers could be mainly addressed to the higher turbulence intensity rather than the more intense local peaks in the jet velocity profile (which are expected to be stronger in the case of $z/d = 0$).

3.2.3 Effect of the Reynolds number (Re)

As already outlined in the previous sections, two different nominal Reynolds number have been tested. Figure 12 (left)

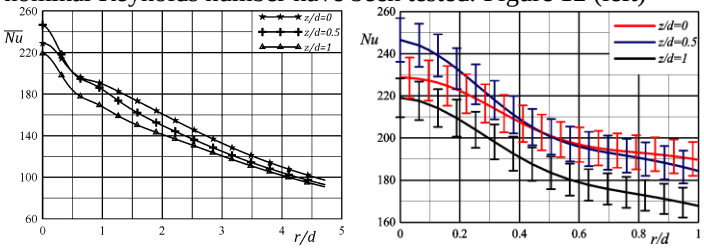

Figure 11 Nusselt number distribution for the FG case at three locations of the grid within the nozzle $z/d = \{0, 0.5, 1\}$ (left) and zoom up to $r/d = 1$(right) with error bars; the nozzle exit-section to plate distance is set to $h/d = 1$; the nominal Reynolds number is 28,700 (see Table 3 for the effective Reynolds number values of the other cases)

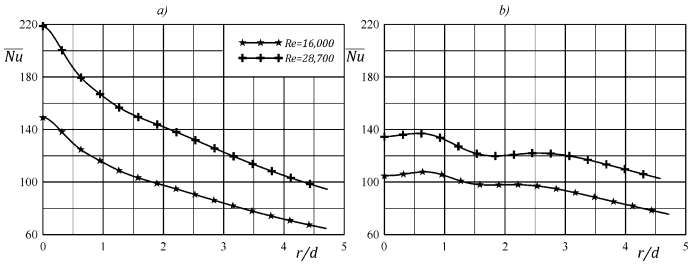

Figure 12 Nusselt number distribution for the FG (a) and JWT (b) cases at two different nominal Reynolds numbers: $Re = 16{,}000, 28{,}700$ (for the JWT $Re = 23{,}200, 38{,}500$) and constant values of the power input equal to 1.1 mW and 5.5 mW.

reports the Nusselt number profiles for the FG case with $h/d = 2$ and $z/d = 0$ (grid placed at the nozzle exit). The increment that is expected as a consequence of the higher upstream Reynolds number reflects on the Nusselt number profiles; in fact, concerning the local maxima, which occur in correspondence of the jet axis, a significant increment can be detected. Considering the correlations available in the literature (see Meola [36] for a review), an increment of the stagnation point Nusselt number of about 42% would be expectable. An improvement of 48% is measured, thus leading to the conclusion that the dependence of the Nusselt number on the Reynolds number is, taking into account also the measurement error, at least equal to the one reported in the literature. On the other hand, by analyzing the profiles for the JWT case (Figure 12, right), for an expected improvement of about 35% (considering that the corresponding Reynolds numbers for the

JWT cases are respectively 23,200 and 38,500), an enhancement of about 31% is measured. In conclusion, the FG results to be more efficient than the JWT for both the tested power input conditions. In both cases, the effect of injecting turbulence within the jet shear layer causes an heat transfer that is much more efficient than the one achievable with a jet without turbulence generators. Whether the enhancement provided by means of fractal stirrers with respect to the JWT is still preserved or not also at higher values of the Reynolds number than those tested, might be addressed to future studies.

DISCUSSION AND CONCLUSIONS

The percentage increments in the Nusselt number obtained for the FG and RG cases with respect to the JWT under the same power input are reported in Table 4 ($Re_d = 28{,}700$, insert placed at the exit section, thus $z/d = 0$). The fractal inserts are extremely efficient turbulent promoters at small nozzle-to-plate distance. Indeed, for $h/d \leq 2$ the improvement in the stagnation region is always greater than 63%, while the regular grid never achieves value beyond 9%. The heat transfer enhancement of the fractal grid drops down significantly for larger nozzle-to-plate distances, but it is still quite appealing (35% at the stagnation region for $h/d = 4$, while for the regular grid the performances are even worse than the JWT under the same power input). The heat transfer rate decay might be addressed both to the fast decay of the turbulent kinetic energy generated by the fractal stirrer and to the spreading of the jet, which smears out the jet velocity peaks generated by the uneven distributed blockage ratio. From the local heat transfer enhancement standpoint, fractal jets are extremely promising. On the other hand, the area-averaged heat transfer rate significantly reduces with the radial distance from the jet. However, for $h/d \geq 3$, the heat transfer rate achieved with a regular insert is always equal or less than that of the JWT under the same power input, while the advantage of using a fractal grid still persists.

In Table 5 the effects of the Reynolds number and of the position of the fractal grid on the heat transfer enhancement are revised. At small distances, it is very interesting to notice that in the stagnation region an improvement in the heat transfer rate is detectable when the grid is set $1d$ within the nozzle. However, as either the radial distance or the separation between the nozzle exit section and the plate increases, placing the grid inside the nozzle reduces significantly the enhancement. As expected, the rapid drop due to the fast turbulence intensity decay is already very sensitive at $h/d \geq 2$ when the insert is at $z/d = 1$. This is due to the larger distance of the turbulator with respect to the plate. Furthermore, when $z/d = 1$ the flow passes through a short pipe segment, which contributes in smearing out the velocity gradients and, consequently, the local accelerations that might be responsible of the heat transfer enhancement.

A lower Reynolds number (data in brackets in Table 5) reduces significantly the stagnation point heat transfer enhancement at small nozzle-to-plate distances. This might be related to the different size of the wakes of the fractal iterations and/or the size of the turbulent eddies contained within them. The outcome of the present analysis is that within the inspected range of Reynolds numbers, the fractal insert is more efficient than the JWT under the same power input. Moreover, when the interest relies in the local enhancement of the heat transfer, positioning the grid within the nozzle carries two benefits: an improvement in the maximum heat transfer and a lower pressure drop. Nevertheless, this aspect exasperates the non-uniformity of the radial distribution of the Nusselt number.

Concluding, the fractal insert causes an improvement on the heat transfer rate, at least locally, whilst, on the downside, reduces the uniformity of the Nusselt number distribution. This aspect opens new paths to the study of possible configurations in order to increase the heat transfer without any loss in terms of uniformity (i.e. twin nozzles configurations). Whether the heat transfer enhancement is achieved due to the non-uniform blockage ratio distribution or by turbulence production mechanism, it is still unexplored, and it will be addressed in future flow field studies.

h/d ($z/d = 0$)	Grid	$\Delta\overline{Nu}$ ($r/D = 0$) %	$\Delta\overline{Nu}$ ($r/D = 1$) %	$\Delta\overline{Nu}$ ($r/D = 2$) %
1	FG	74	45	33
	RG	29	23	17
2	FG	63	25	19
	RG	9	6	5
3	FG	46	17	11
	RG	-1	-1	-1
4	FG	35	11	5
	RG	-4	-4	-4

Table 4 Nusselt number increment of the FG and RG cases with respect to the JWT case at four different nozzle to plate distances and three different radial locations; the test conditions are: nominal $Re = 28{,}700$ and $z/d = 0$ (for the effective Reynolds number see Table 3)

h/d	z/d	$\overline{Nu}$ ($r/D = 0$)	$\overline{Nu}$ ($r/D = 1$)	$\overline{Nu}$ ($r/D = 2$)
1	0	74 (48)	45 (22)	33 (7)
	0.5	87 (56)	41 (18)	22 (-1)
	1	66 (50)	29 (12)	15 (-4)
2	0	63 (42)	25 (10)	19 (0.3)
	0.5	41 (31)	14 (2)	5 (-10)
	1	24 (26)	8 (2)	1 (-10)
3	0	46 (28)	17 (3)	11 (-4)
	0.5	21 (11)	5 (-7)	-2 (-14)
	1	6 (7)	-3 (-6)	-8 (-13)
4	0	35 (16)	11 (-3)	5 (-7)
	0.5	8 (-3)	-3 (-12)	-9 (-16)
	1	3 (-7)	-9 (-13)	-13 (-20)

Table 5 Heat transfer rate enhancement at three radial locations ($\frac{r}{d} = \{0, 1, 2\}$) using the fractal insert at three different locations within the nozzle $z/d = \{0, 0.5, 1\}$; data in the brackets refer to a different nominal Reynolds number $Re = 16{,}800$.

REFERENCES

[1] Martin H (1977) Heat and Mass Transfer Between Impinging Gas Jets and Solid Surfaces. Advances in Heat Transfer 13:1-60.

[2] Polat S, Huang B, Mujumdar AS, Douglas WJW (1989) Numerical flow and heat transfer under impinging jets: a review. Annual Review of Heat Transfer 2:157–197.

[3] Viskanta R (1993) Heat-transfer to impinging isothermal gas and flame jets, Experimental Thermal Fluid Science 6:111–134.

[4] Jambunathan K, Lai E, Moss MA, Button BL (1992) A review of heat transfer data for a single circular jet impingement- International Journal of Heat and Fluid Flow 13:106–115.
[5] O'Donovan TS, Murray DB (2007) Jet impingement heat transfer – Part I: Mean and root-mean-square heat transfer and velocity distributions. International Journal of Heat and Mass Transfer 50:3291–3301.
[6] Liu TS, Sullivan JP (1996) Heat transfer and flow structures in an excited circular impinging jet. International Journal of Heat and Mass Transfer 39:3695–3706.
[7] Ward J, Mahmood M (1982) Heat Transfer from a Turbulent, Swirling, Impinging Jet, Heat Transfer 3:401-408.
[8] Huang L, El-Genk MS (1998) Heat transfer and flow visualization experiments of swirling, multi-channel, and conventional impinging jets. International Journal of Heat and Mass Transfer 41:583-600.
[9] Ianiro A, Cardone G (2012) Heat transfer rate and uniformity in multichannel swirling impinging jets. Applied Thermal Engineering 49:89-98.
[10] Lee DH, Lee YM, Kim YT, Won SY, Chung YS (2002) Heat transfer enhancement by the perforated plate installed between an impinging jet and the target plate. International Journal of Heat and Mass Transfer 45:213–217.
[11] Zhou DW, Lee SJ (2004) Heat transfer enhancement of impinging jets using mesh screens. International Journal of Heat and Mass Transfer 47:2097–2108.
[12] Zhou DW, Lee SG, Ma CF, Bergles AE (2006) Optimization of mesh screen for enhancing jet impingement heat transfer. Heat and Mass Transfer 42: 501–510.
[13] Kataoka K, Suguro M, Degawa H, Maruo K, Mihata I (1987) Effect of Surface Renewal Due to Large-Scale Eddies on Jet Impingement Heat Transfer. International Journal of Heat and Mass Transfer 30:559-567, 1987.
[14] Kataoka K (1990) Impingement Heat Transfer Augmentation Due to Large Scale Eddies, Heat Transfer 1:255-273.
[15] Gardon R, Akfirat JC (1964) Heat Transfer Characteristics of Impinging Two-Dimensional Air Jets. Journal of Heat Transfer 86:101-108.
[16] Hoogendoorn CJ (1977) The effect of turbulence on heat transfer at a stagnation point. International Journal of Heat and Mass Transfer 20:1333–1338.
[17] Smith M, Kuethe A (1966) Effects of turbulence on laminar skin friction and heat transfer, Physics of Fluids 9:2337-2344.
[18] Gardon R, Akfirat, JC (1965) The Role of Turbulence in Determining the Heat Transfer Characteristics of Impinging Jets. International Journal of Heat and Mass Transfer 8:1261-1272.
[19] Gori F, Petracci I (2012) Influence of turbulence on heat transfer upon a cylinder impinged by a slot jet of air. Applied Thermal Engineering 49:106-117.
[20] Hurst D, Vassilicos JC (2007) Scalings and decay of fractal-generated turbulence. Physics of Fluids 19, 035103.
[21] Mazellier N, Vassilicos JC (2010) Turbulence without Richardson–Kolmogorov cascade. Physics of fluids 22,075101.
[22] Taylor GI (1935) Statistical theory of turbulence Proc. R. Soc. Lond. A 151 421–44
[23] Kolmogorov AN (1941) The local structure of turbulence in incompressible viscous fluid for very large Reynolds C. R. Acad. Sci. 30 301–5
[24] Seoud RE, Vassilicos JC (2007) Dissipation and decay of fractal-generated turbulence. Physics of Fluids 19, 105108.
[25] Valente PC, Vassilicos JC (2011) The decay of turbulence generated by a class of multiscale grids. Jorunal of Fluid Mechanics 687:300-340.
[26] Discetti S, Ziskin IB, Astarita T, Adrian RJ, Prestridge K (2013) PIV measurements of anisotropy and inhomogeneity in decaying fractal generated turbulence. Fluid Dynamics Research 45, 061401.
[27] Geipel P, Goh KHH, Lindstedt RP (2010) Fractal-Generated Turbulence in Opposed Jet Flows. Flow, Turbulence and Combustion 85:397–419.
[28] Kinzel M, Wolf M, Holzner M, Lüthi B, Tropea C, Kinzelbach W (2011) Simultaneous two-scale 3D-PTV measurements in turbulence under the influence of system rotation. Experiments in Fluids 51:75-82.
[29] Laizet S and Vassilicos JC (2012) Multi-scale unfolding mechanism for energy-efficient turbulent mixing. Physical Review Letter E 86:046302.
[30] Astarita T, Carlomagno GM (2013) Infrared Thermography for Thermo-Fluid-Dynamics. Springer Ed., Berlin, ISBN: 9783642295072.
[31] Incropera FP, Lavine AS, Theodore TL, DeWitt DP (2011) Fundamentals of Heat and Mass Transfer. John Wiley & Sons.
[32] McAdams WH (1954) Heat transmission, 3rd Edition McGraw-Hill, New York, NY.
[33] Astarita T, Cardone G, Carlomagno GM (2006) Infrared Thermography: An optical method in heat transfer and fluid flow visualization. Optics and Lasers in Engineering 44: 261-281.
[34] Carlomagno GM, Discetti S, Astarita T (2011) Experimental assessment of a new heat flux sensor for measuring convective heat transfer coefficients. QIRT J 8:37-49.
[35] Moffat RJ (1988) Describing the Uncertainties in Experimental Results. Experimental Thermal and Fluid Science 1:3-17.
[36] Meola C (2009) A New Correlation of Nusselt Number for Impinging Jets. Heat Transfer Engineering 30:221-228.